

## GENETICS

# The synaptonemal complex aligns meiotic chromosomes by wetting

Spencer G. Gordon<sup>1</sup>, Alyssa A. Rodriguez<sup>2</sup>, Yajie Gu<sup>2</sup>, Kevin D. Corbett<sup>2,3</sup>, Chiu Fan Lee<sup>4</sup>, Ofer Rog<sup>1\*</sup>

During meiosis, the parental chromosomes are drawn together to enable exchange of genetic information. Chromosomes are aligned through the assembly of a conserved interface, the synaptonemal complex, composed of a central region that forms between two parallel chromosomal backbones called axes. Here, we identify the axis-central region interface in *C. elegans*, containing a conserved positive patch on the axis component HIM-3 and the negative C terminus of the central region protein SYP-5. Crucially, the canonical ultrastructure of the synaptonemal complex is altered upon weakening this interface using charge-reversal mutations. We developed a thermodynamic model that recapitulates our experimental observations, indicating that the liquid-like central region can assemble by wetting the axes without active energy consumption. More broadly, our data show that condensation drives tightly regulated nuclear reorganization during sexual reproduction.

## INTRODUCTION

Cellular processes are tightly controlled spatially, requiring that large structures, such as organelles or chromosomes, be moved and precisely positioned. This is most commonly achieved by motor proteins and the polymerization/depolymerization of cytoskeletal filaments. These active processes consume free energy provided by the hydrolysis of nucleotide triphosphate (NTP) molecules to move cargo over large distances. However, an alternative mechanism that could regulate cellular organization has been proposed: thermodynamically driven formation of protein assemblies (1). Biomolecular condensates interact with membrane-bound organelles and other large cellular structures (2), and synthetic condensates are capable of exerting pico-newton-scale forces on adjacent structures (3). However, the functional importance of condensate assembly for moving cellular structures in vivo remains unclear.

A cellular structure whose maneuvering is particularly well-regulated is the chromosome. During meiosis, the specialized cell division cycle that produces gametes, the unassociated homologous parental chromosomes (homologs) are brought together and aligned along their lengths (4). Paired and aligned homologs are necessary for the formation of exchanges (crossovers) that shuffle the maternal and paternal genomes and allow chromosomes to correctly segregate into the gametes. Errors in these intricate processes lead to aneuploidy, congenital birth defects, and infertility.

Chromosome alignment in meiosis is driven and controlled by the synaptonemal complex—a conserved protein structure that assembles between homologs. The structure is built from two main elements—axes and the synaptonemal complex central region (SC-CR; Fig. 1, A and B). The axes are composed of cohesins and HORMA-domain proteins, which mold the chromosome into an array of loops (the acronym HORMA stands for the three proteins it was initially identified in: Hop1, Rev7 and Mad2). The SC-CR, made of coiled-coil proteins, associates with preassembled axes on the two homologs, placing them parallel to one another and ~150 nm apart.

Synaptonemal complex assembly, or synapsis, extends localized pairing interactions to align the homologs end-to-end and intimately juxtapose homologous sequences. The synaptonemal complex also directly regulates factors that form crossover (5), potentially by regulating their diffusion along chromosomes (6–10).

The mechanism of synaptonemal complex assembly remains unknown. Such a mechanism must account not only for the reorganization of the nucleus—dragging and aligning the massive structures that are chromosomes—but also for the ability of the synaptonemal complex to dynamically respond to local and large-scale cues, such as karyotype alterations and crossovers (4, 5, 11). The ladder-like appearance of the SC-CR in negative-stained electron micrographs (Fig. 1A), the stereotypic organization of subunits within the SC-CR (Fig. 1B) (12–14), and its assembly through processive extension (15, 16) all contributed to the idea that assembly proceeds through zipping. This mode of assembly would be similar to active polymerization of cytoskeletal filaments, which locally consume free energy generated by NTP hydrolysis to stably attach subunits at the growing end. The tight interactions that underlie zipping could account for the ability of the synaptonemal complex to resist the restoring force of chromatin. Synaptonemal complex dynamics in this regime could be achieved by dedicated machinery that locally modulates subunit affinity to allow dis- and reassembly. The more recent observations of constant SC-CR subunit exchange within the synaptonemal complex and of fluid behaviors exhibited by the SC-CR suggest that it is a biomolecular condensate with liquid properties (10, 17–19). The synaptonemal complex may therefore assemble by condensation of the SC-CR between parallel axes, moving chromosomes by capillary-like forces. Condensation is brought about by an ensemble of multivalent interactions that can together create strong avidity and hold chromosomes together. At the same time, these relatively weak self-interactions provide an elegant mechanism to enable local rearrangement without requiring additional regulators.

Unfortunately, available tools to reconstitute, perturb, and image the synaptonemal complex have failed to distinguish between possible assembly mechanisms. Underlying these challenges is the inability to modulate the interactions between the SC-CR and the axis, since the molecular contacts between them are not known (20). Here, we identify components of the axis–SC-CR interface in the nematode *Caenorhabditis elegans*, comprising a conserved positive

Copyright © 2025 The Authors, some rights reserved; exclusive licensee American Association for the Advancement of Science. No claim to original U.S. Government Works. Distributed under a Creative Commons Attribution NonCommercial License 4.0 (CC BY-NC).

<sup>1</sup>School of Biological Sciences and Center for Cell and Genome Sciences, University of Utah, Salt Lake City, UT 84112, USA. <sup>2</sup>Department of Cellular and Molecular Medicine, University of California San Diego, La Jolla, CA 92093, USA. <sup>3</sup>Department of Molecular Biology, University of California San Diego, La Jolla, CA 92093, USA. <sup>4</sup>Department of Bioengineering, Imperial College London, London, UK.

\*Corresponding author. Email: ofer.rog@utah.edu

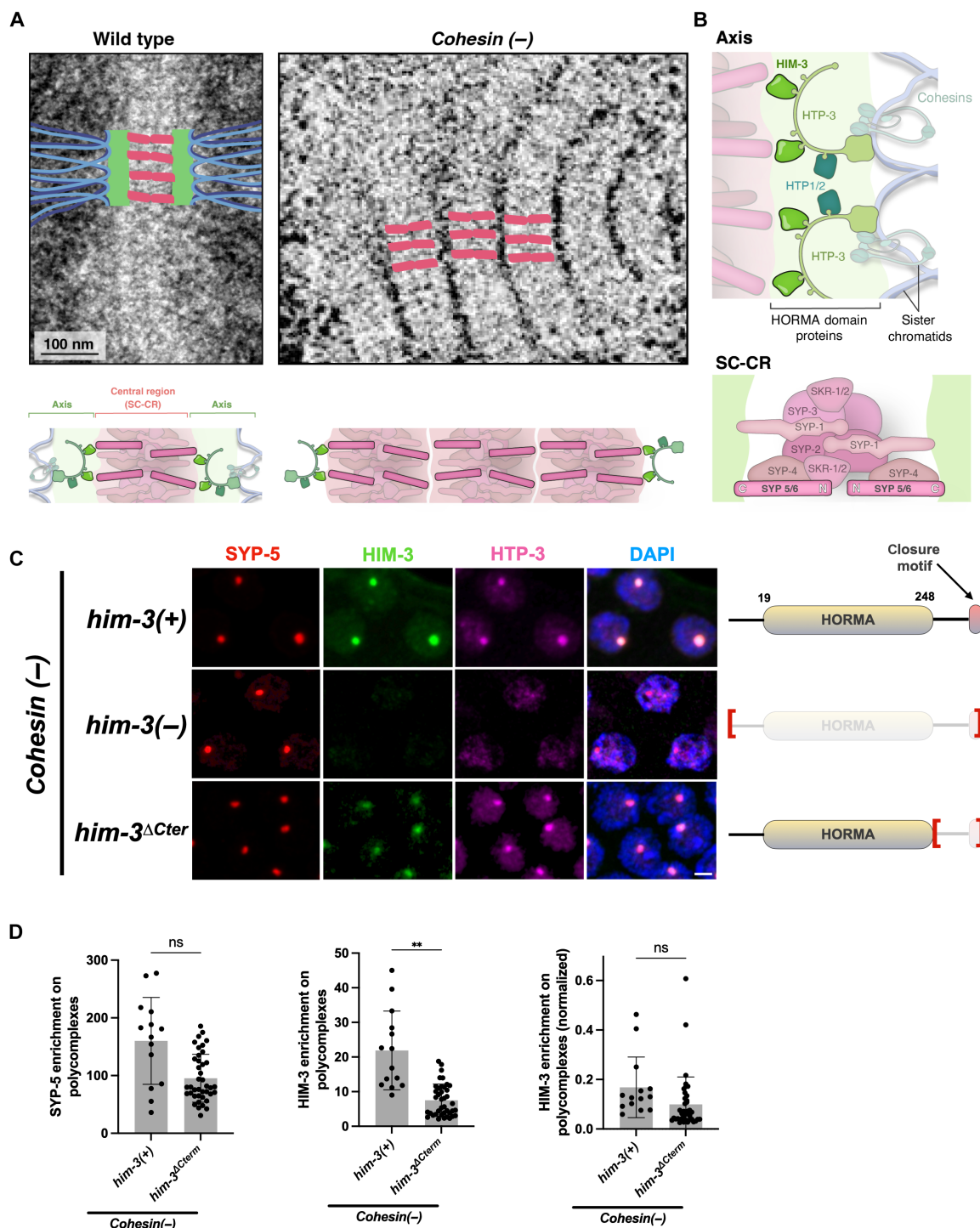


**Fig. 1. The HORMA domain of HIM-3 is required for axis interactions with the SC-CR.** (A) Top left: Assembled synaptonemal complex with the darkly stained parental chromosomes to its side (left) and of the polycomplexes that form in *cohesin(-)* worms (right) as seen in negative negative stain electron micrographs [adapted from (17)]. Bottom left: Interpretive diagrams colored magenta for the SC-CR, green for the axes (also called lateral or axial elements), and blue for chromatin. (B) Models depicting the worm components of the axis (top) and the SC-CR (bottom). The position of each of these components within the synaptonemal complex is based on (12, 25, 29, 30, 51). The pairs HTP-1/2, SYP-5/6, and SKR-1/2 are each partially redundant with each other. (C) Pachytene nuclei from worms of the indicated genotypes stained for the SC-CR component SYP-5 (red) and the axis components HIM-3 (green) and HTP-3 (magenta). The merged images on the right also show DNA [4',6-diamidino-2-phenylindole (DAPI), blue]. The HTP-3 antibody weakly cross-reacts with the nucleolus. Scale bar, 1  $\mu$ m. Gene models of HIM-3, with the HORMA domain and the closure motif highlighted, are shown to the right. Regions deleted are denoted by red brackets. See fig. S1A for images of the gonads. (D) Quantification of the images in (C). The enrichment at polycomplexes relative to the nucleoplasm was done using line scans. Normalized HIM-3 enrichment was calculated by dividing HIM-3 enrichment by SYP-5 enrichment.  $N = 14$  and 40 for *him-3<sup>+</sup>* and *him-3<sup>ΔCterm</sup>*. Brown-Forsythe and Welch analysis of variance (ANOVA)  $P = 0.09$ , 0.005, and 0.64 for SYP-5, HIM-3, and HIM-3 (normalized). ns, not significant.

patch on the axis protein HIM-3 and the negative C terminus of the SC-CR protein SYP-5. The positive patch on HIM-3 interacts with SYP-5 in vivo and in vitro to mediate synaptonemal complex assembly. The effects of weakened axis–SC-CR interactions on the morphology of the synaptonemal complex support SC-CR assembly through wetting. To demonstrate the feasibility of this idea, we generated a thermodynamic model. Our model assumes no local consumption of free energy and relies on the condensation of SC-CR molecules and on surface binding of SC-CR components to the axis to recapitulate the experimentally observed phenotypes of meiotic perturbations.

## RESULTS

### The axis protein HIM-3 is a component of the axis–SC-CR interface

To identify the axis–SC-CR interface, we wanted to study this interface independently of other mechanisms that affect chromosome organization. We used polycomplexes: assemblies of SC-CR material that form when the SC-CR cannot load onto chromosomes. Since the stacked SC-CR lamellae in polycomplexes closely resemble the SC-CR layer that forms between the axes under physiological conditions, polycomplexes have been used to study SC-CR ultrastructure (21, 22). We used worms that lack meiotic cohesins [deletion of the meiotic kleisins *rec-8* and *coh-3/4*, designated *cohesin*(–)], which prevents axis assembly onto chromosomes. In these worms, SC-CR material forms chromatin-free polycomplexes that recruit axis components [Fig. 1, A and C, and fig. S1B; (17, 23); throughout, polycomplexes are marked by labeling the SC-CR components SYP-1, SYP-2, SYP-3, or SYP-5, which exhibit indistinguishable localization patterns].

First, we wanted to identify the axis components required for polycomplex-axis interactions. Of the four meiotic HORMA proteins in worms—HTP-3, HIM-3, and HTP-1/2—we predicted a crucial role for HIM-3 based on its proximity to the SC-CR and the increasing synapsis defects upon its gradual removal (20, 24, 25). Upon deletion of *him-3*, the axis components HTP-3 and HTP-1/2 failed to localize to polycomplexes, as revealed by immunostaining (Fig. 1C and fig. S1C). This suggests that HIM-3 may directly interact with the SC-CR, whereas HTP-3 and HTP-1/2 are recruited to polycomplexes indirectly, through interactions with HIM-3 (26). Sequential deletions of HIM-3 regions showed that the C terminus of HIM-3, which includes a disordered linker and a domain that interacts with other HORMA proteins (called the “closure motif”), plays only a minimal role in the recruitment of axis proteins to polycomplexes (Fig. 1, C and D). This result suggested that the SC-CR–interacting region lies in the HORMA domain of HIM-3.

The HORMA domain is a conserved fold shared among meiotic axis proteins (27). We examined the structures of the HORMA domains in the three meiotic axis proteins—HIM-3, HTP-3, and HTP-1/2 [Fig. 2A; (26)]—to identify divergent surfaces that could mediate HIM-3’s specific contribution to axis–SC-CR interactions. We noticed a positively charged patch on HIM-3, containing lysines at positions 170, 171, 177, and 178 and an arginine at position 174 (Fig. 2A and fig. S2A). This positive patch is unique to HIM-3 among *C. elegans* HORMA proteins, but a similar positive patch is also present in HORMA-domain containing axis proteins in other species (fig. S2B). Specifically, HORMA axis proteins in budding yeast and animals have a pair of positively charged residues that align

with lysines 170 and 171 on HIM-3. In addition, positively charged residues are present in other solvent-exposed positions of the same  $\alpha$  helix, such as the residues homologous to lysine 162 on HIM-3. Structural analysis confirmed that positively charged residues in *Saccharomyces cerevisiae* Hop1 (arginines 175 and 176) and human HORMAD1 (arginine 155 and lysine 156) occupy an equivalent position to lysines 170 and 171 on HIM-3 (fig. S2C).

We generated several HIM-3 mutants that reversed the charge in the positive patch (Fig. 2A). These mutations decreased the accumulation of HIM-3 on polycomplexes: ~4-fold for *him-3*<sup>R174E</sup> and reduction to almost background level for *him-3*<sup>KK170-171EE</sup> and *him-3*<sup>KK177-178EE</sup> [Fig. 2, B to E; in (E), we normalized HIM-3 enrichment relative to SYP-5 enrichment]. The indirect recruitment of HTP-3 to polycomplexes was also abolished. Analysis in live *cohesin*(–) gonads, using green fluorescent protein (GFP)–tagged HIM-3, yielded similar results (fig. S3; ~5-fold reduction for *gfp-him-3*<sup>R174E</sup> versus *gfp-him-3* worms). These data indicate that the positive patch on HIM-3 mediates association with SC-CR components.

### The HIM-3 positive patch is essential for synaptonemal complex assembly

To assess the contribution of the HIM-3 positive patch to synapsis, we analyzed meiosis in our HIM-3 positive patch mutants. Worms harboring *him-3*<sup>R174E</sup> and *him-3*<sup>KK170-171EE</sup> exhibited disrupted meiosis, consistent with their relative disruption of axis–SC-CR interactions. The *him-3*<sup>R174E</sup> worms had only 21 progeny on average, as compared with 300 progeny for wild-type worms, with 4.2% male self-progeny, indicative of missegregation of the X chromosome (Fig. 3, A and B; wild-type worms have 0.1% male progeny). These defects were much more severe in *him-3*<sup>KK170-171EE</sup> worms, which exhibited phenotypes similar to *him-3* null worms (28) and were almost sterile.

Cytological examination indicated that an average of 3.2 of the six chromosome pairs synapsed in *him-3*<sup>R174E</sup> worms and only 1.5 chromosomes synapsed in *him-3*<sup>KK170-171EE</sup> worms (Fig. 3, C and D, and fig. S4A). The synapsed chromosomes appear to form cross-overs, as indicated by the correspondence between the number of synapsed chromosomes and the number of chromosomes attached through chiasmata (Fig. 3E). The residual association of SC-CR material with axes in *him-3*<sup>KK170-171EE</sup> worms suggests that other axis components may harbor a weak affinity for the SC-CR. Consistent with this idea, chromosomes with axes that lack HIM-3 altogether are still associated with SC-CR material [(26); see also Fig. 3F].

HIM-3 positive patch mutant proteins still loaded onto both synapsed and asynapsed chromosomes (Fig. 3C). Total HIM-3 levels and the fraction of HIM-3 on chromosomes were also minimally affected in the mutants (fig. S4, B to D). These data suggest that the surface charge alterations in *him-3* are bona fide separation-of-function mutations and that the phenotypes they exhibit can be attributed to disrupted axis–SC-CR interactions.

### Disrupting axis–SC-CR interactions alters synaptonemal complex morphology

To gain better insight into the morphology of the synaptonemal complex in *him-3* mutants, we used stimulated emission-depletion super-resolution microscopy (STED). The axes in wild-type worms, and in most synapsed chromosomes in *him-3*<sup>R174E</sup> worms, exhibited the canonical layered ultrastructure of an assembled synaptonemal complex: They were parallel along their length, separated by



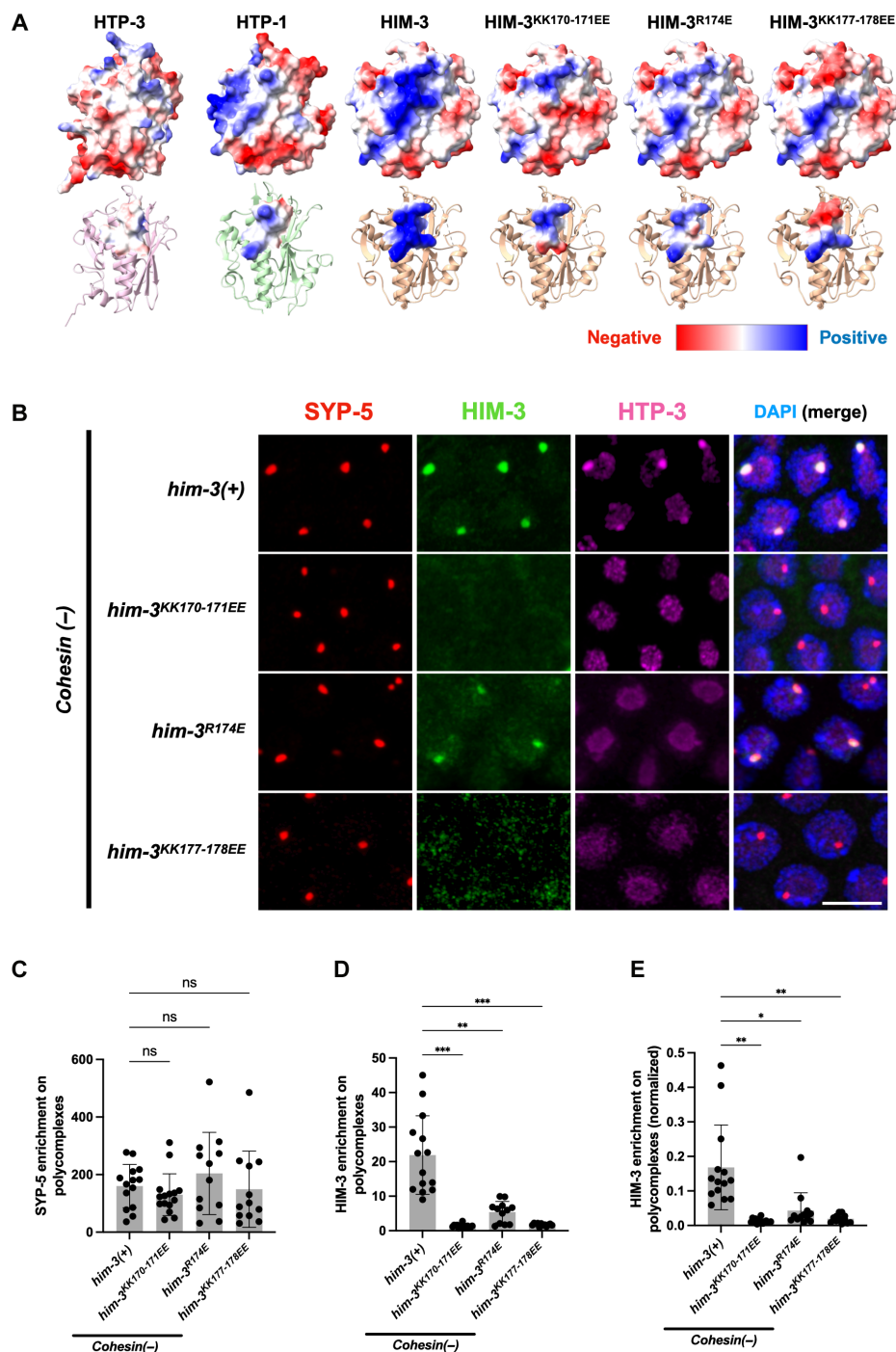


**Fig. 2. Axis interactions with the SC-CR are mediated by a positive patch on the HORMA domain of HIM-3.** (A) Structural models of the meiotic HORMA proteins, with surface charge plotted in a red-blue scale. The structures of HTP-1 and HIM-3 are from (26). The models of HTP-3 and the three HIM-3 mutants were generated in AlphaFold (45). Bottom: Secondary structural models, with amino acids constituting the positive patch on HIM-3 (positions 170, 171, 174, 177, and 178), and the analogous positions in HTP-1 and HTP-3 are shown as surfaces colored according to charge. Note that the positive patch on HIM-3 is located away from the closure motif binding pocket; see fig. S2A. (B) Pachytene nuclei from worms of the indicated genotypes stained for the SC-CR component SYP-5 (red) and the axis components HIM-3 (green) and HTP-3 (magenta). The merged images on the right also show DNA (DAPI, blue). The HTP-3 antibody weakly cross-reacts with the nucleolus. Scale bar, 1  $\mu$ m. See fig. S2D for images of the gonads and fig. S3 for similar analysis in live gonads. (C to E) Quantification of the images in (B). The enrichment at polycomplexes relative to the nucleoplasm was done using line scans. Normalized enrichment (E) was calculated by dividing HIM-3 enrichment by SYP-5 enrichment.  $N = 14, 15, 12$ , and  $12$  for *him-3(+)*, *him-3<sup>KK170-171EE</sup>*, *him-3<sup>R174E</sup>*, and *him-3<sup>KK177-178EE</sup>*. (C) Brown-Forsythe and Welch ANOVA  $P[\text{him-3}(+) \text{ versus } \text{him-3}^{\text{KK170-171EE}}] = 0.99$ ;  $P[\text{him-3}(+) \text{ versus } \text{him-3}^{\text{R174E}}] = 0.99$ ;  $P[\text{him-3}(+) \text{ versus } \text{him-3}^{\text{KK177-178EE}}] > 0.99$ . (D) Brown-Forsythe and Welch ANOVA  $P[\text{him-3}(+) \text{ versus } \text{him-3}^{\text{KK170-171EE}}] = 0.0002$ ;  $P[\text{him-3}(+) \text{ versus } \text{him-3}^{\text{R174E}}] = 0.0015$ ;  $P[\text{him-3}(+) \text{ versus } \text{him-3}^{\text{KK177-178EE}}] = 0.0002$ . (E) Brown-Forsythe and Welch ANOVA  $P[\text{him-3}(+) \text{ versus } \text{him-3}^{\text{KK170-171EE}}] = 0.0053$ ;  $P[\text{him-3}(+) \text{ versus } \text{him-3}^{\text{R174E}}] = 0.036$ ;  $P[\text{him-3}(+) \text{ versus } \text{him-3}^{\text{KK177-178EE}}] = 0.0078$ .



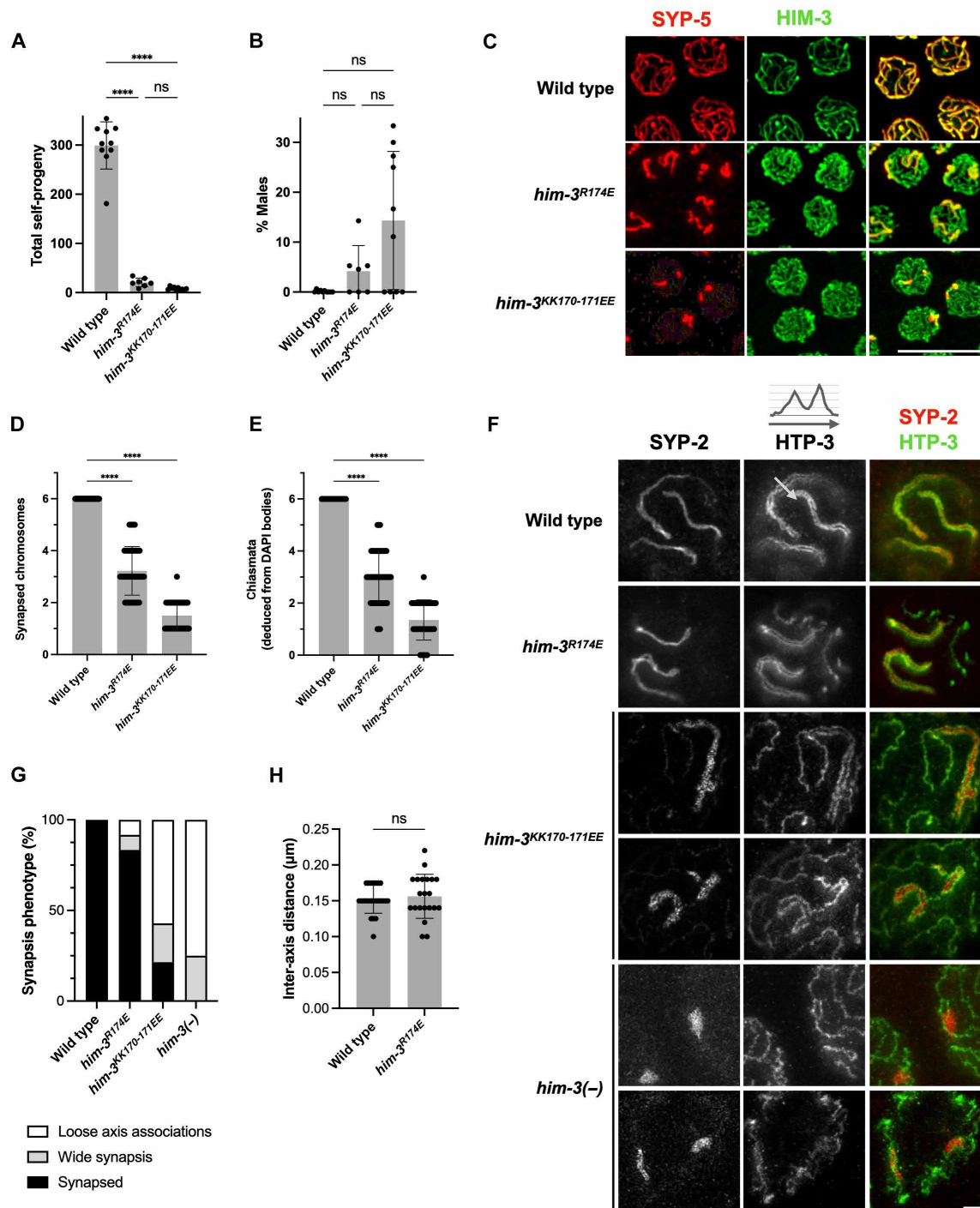


**Fig. 3. Lowering SC-CR affinity for the axes perturbs synapsis.** (A) Total self-progeny from hermaphrodites of the indicated genotypes. (B) Percentage of males among self-progeny of hermaphrodites of the indicated genotypes, indicative of meiotic X chromosome non-disjunction. (C) Pachytene nuclei stained for the SC-CR component SYP-5 (red) and the axis component HIM-3 (green), with merged images shown on the right. Note the extensive asynapsis in the *him-3* mutants (i.e., axes lacking SC-CR staining) despite loading of the mutated HIM-3 proteins onto the axis. Scale bar, 10  $\mu$ m. See fig. S4A for images of the gonads. (D) Quantification of the images in (C), indicating a smaller number of synapsed chromosomes in *him-3* mutants. (E) Chiasmata number deduced from the number of DAPI bodies at diakinesis. Wild-type animals undergo one chiasma per chromosome, for a total of six chiasmata per nucleus. (F) STED microscopy images of pachytene nuclei stained for the SC-CR component SYP-2 (red in the merged image) and the axis component HTP-3 (green in the merged image). An example of a line scan through a synapsed chromosome is shown above the HTP-3 staining in wild-type animals. Scale bar, 1  $\mu$ m. (G) Quantification of different synapsis phenotypes in STED images, as shown in (F). "Wide synapsis" indicates parallel axes separated by more than 150 nm, as shown in the top nucleus from *him-3<sup>KK170-171EE</sup>* animals. "Loose axis associations" indicate axes wrapped around SC-CR structures, as shown in the bottom nucleus from *him-3<sup>KK170-171EE</sup>* animals. (H) Inter-axes distance in the indicated genotypes, measured from nuclei stained as in (F). Distance was measured only between parallel axes that had unilamellar SYP-2 staining. See Materials and Methods for full statistical information. \*\*\*\* $P \leq 0.0001$ .

~150 nm [Fig. 3, F to H; note that axes are marked using antibodies against the axis component HTP-3, whose localization to chromosomes is independent of HIM-3; (4, 11, 26)]. *him-3<sup>KK170-171EE</sup>* and *him-3(-)* chromosomes, however, were much more disorganized. Axes were often associated with each other without being parallel, and even seemingly aligned axes failed to maintain a 150-nm spacing (Fig. 3G). In some cases, SC-CR aggregates interacted with multiple axes—a situation never observed in wild-type worms (Fig. 3, F and G).

Staining a protein that localizes in the middle of the SC-CR [SYP-2; Fig. 1B; (12, 13)] revealed that many of the SC-CR structures in *him-3<sup>KK170-171EE</sup>* worms do not form the single thread observed in wild-type animals, implying that the inter-axes space is occupied by more than a single lamella of SC-CR (Fig. 3F). Instead, the SYP-2 epitope exhibited a dotted appearance with some parallel threads (Fig. 3F and fig. S5). Measurements in live worms confirmed the presence of many more SC-CR molecules per chromosome in *him-3<sup>KK170-171EE</sup>* worms compared with wild-type or *him-3<sup>R174E</sup>* worms (fig. S11F). This pattern is reminiscent of polycomplexes, which resemble stacked SC-CR lamellae, with a distance between the center of each lamella (where SYP-2 localizes) similar to the width of native synaptonemal complex [fig. S5; (17, 21)].

Together, our analyses indicate that HIM-3-mediated axis-SC-CR interactions drive synaptonemal complex assembly. Furthermore, the altered SC-CR morphology in *him-3* mutants sheds light on the mechanism of synapsis, pointing to an interplay between axis-SC-CR interactions and self-interactions among SC-CR subunits. Below, we use this understanding to generate a thermodynamic model for synaptonemal complex assembly.

### The SC-CR protein SYP-5 interacts with the HIM-3 positive patch

To identify SC-CR components that interact with the HIM-3 positive patch, we searched the worm SC-CR subunits—SYP-1-6 and SKR-1/2—to identify those that harbor negatively charged regions that localize near the axes. An attractive candidate was SYP-5, which has a negatively charged C terminus that localizes near the axes and, when mutated, leads to synapsis defects [Fig. 1B; (29–31)]. (The C terminus of SYP-1, which also localizes near the axes, is not negatively charged.)

We generated two charge-reversal mutants in *syp-5* (*syp-5<sup>5K</sup>* and *syp-5<sup>6K</sup>*, mutating five and six aspartic and glutamic acids to lysines, respectively; Fig. 4A). We analyzed them in the *cohesin(-)* *him-3<sup>KK170-171EE</sup>* background, hypothesizing that charge swap may restore the recruitment of axis components to polycomplexes. We found that polycomplexes in *cohesin(-)* *him-3<sup>KK170-171EE</sup>* *syp-5<sup>5K</sup>* worms recruited significantly more HIM-3 compared to *cohesin(-)* *him-3<sup>KK170-171EE</sup>* controls (Fig. 4, B to E; note that we used antibodies against SYP-2 to mark polycomplexes to exclude any effect of the mutations in *syp-5* on recognition by anti-SYP-5 antibodies). This likely underestimates the effect of *syp-5<sup>5K</sup>* on axis-SC-CR interactions, since polycomplexes in this background concentrated less SC-CR, likely due to impaired SC-CR self-interactions [Fig. 4C and fig. S11B; (30)]. The *syp-5<sup>6K</sup>* mutation further weakened SC-CR self-interactions, completely preventing polycomplex formation in *cohesin(-)* *him-3<sup>KK170-171EE</sup>* worms and precluding assessment of its effect on axis-SC-CR interactions (Fig. 4B). These data suggest that the C terminus of SYP-5 contributes to axis-SC-CR interactions, in addition to promoting self-interactions between SC-CR subunits.

When we analyzed *him-3<sup>KK170-171EE</sup>* *syp-5<sup>5K</sup>* and *him-3<sup>KK170-171EE</sup>* *syp-5<sup>6K</sup>* worms, we found only one or two SC-CR-associated chromosomes per nucleus, similar to *him-3<sup>KK170-171EE</sup>* worms (Fig. 4, F and G, and fig. S6B). Crucially, however, the synaptonemal complex on these synapsed chromosomes exhibited morphologies more similar to wild type. This effect was the strongest for *him-3<sup>KK170-171EE</sup>* *syp-5<sup>6K</sup>* worms, where almost all the synaptonemal complexes exhibited a canonical morphology: a single SC-CR thread between the axes and an inter-axis distance of ~150 nm (Fig. 4, H and I).

When analyzed by themselves, both *syp-5<sup>5K</sup>* and *syp-5<sup>6K</sup>* worms exhibited defects in synaptonemal complex assembly (fig. S7, A and B). These defects included the presence of asynapsed chromosomes and chromosomes that failed to form a crossover, as well as consequent defects in chromosome segregation leading to reduced progeny number and a higher prevalence of male self-progeny. Consistent with its stronger effect on synaptonemal complex morphology in *him-3<sup>KK170-171EE</sup>* worms, *syp-5<sup>6K</sup>* worms exhibited stronger defects compared with *syp-5<sup>5K</sup>* worms.

To confirm that HIM-3 interacts directly with the C terminus of SYP-5, we expressed and purified a complex of HTP-3 bound to multiple HIM-3 molecules (26) and tested binding to a peptide spanning residues 528 to 547 of SYP-5. We also tested binding of the HTP-3-HIM-3 complex to a SYP-5 peptide phosphorylated at serine 541; phosphorylation of this site by polo-like kinases was recently suggested to be important for synapsis (31). HIM-3 strongly interacted with the phosphorylated SYP-5 peptide (Fig. 4J and fig. S8). This interaction was much weaker with unphosphorylated SYP-5 peptide, further underscoring the importance of this modification (31). HTP-3 alone did not interact with the SYP-5 peptides, demonstrating that HIM-3 is required for this interaction (fig. S8), consistent with our analysis of polycomplexes (Fig. 1).

The interaction between HIM-3 and the SYP-5 peptides was markedly reduced upon charge reversal mutations in the HIM-3 positive patch. *HIM-3<sup>R174E</sup>*, *HIM-3<sup>KK170-171EE</sup>*, and *HIM-3<sup>KK177-178EE</sup>* copurified with HTP-3 at similar levels (fig. S8), consistent with the ability of charge reversal mutants to assemble axes in vivo (Fig. 3 and fig. S4). However, the three mutants exhibited reduced binding to the SYP-5 peptides, demonstrating the specificity of HIM-3-SYP-5 interaction and the importance of the positive charge. Together with our in vivo data, we conclude that axis-SC-CR interactions are mediated by direct interaction between the positive patch on HIM-3 and the C terminus of SYP-5 to promote synaptonemal complex assembly.

### Thermodynamic model of synaptonemal complex assembly

Our analysis of *him-3* mutants helps differentiate between different mechanisms of synaptonemal complex assembly. Zipping-based mechanisms predict that disrupting axis-SC-CR interactions will not affect interactions between SC-CR subunits or prevent zipping per se. Rather, the effect on alignment of the axes (and the chromosomes) will be mediated by, for instance, decoupling the axes from the SC-CR or premature termination of SC-CR zipping. Thermodynamically driven assembly makes a different prediction. To assemble, attractive self-interactions and surface binding to the axes act together to drive condensation, which overcomes the entropic-driven dispersion of SC-CR components and chromosomes. It is therefore both these interactions that determine the morphology of the synaptonemal complex. Our observations in *him-3<sup>KK170-171EE</sup>* worms support thermodynamically driven assembly: The weakened axis-SC-CR interactions led to the formation of a much thicker

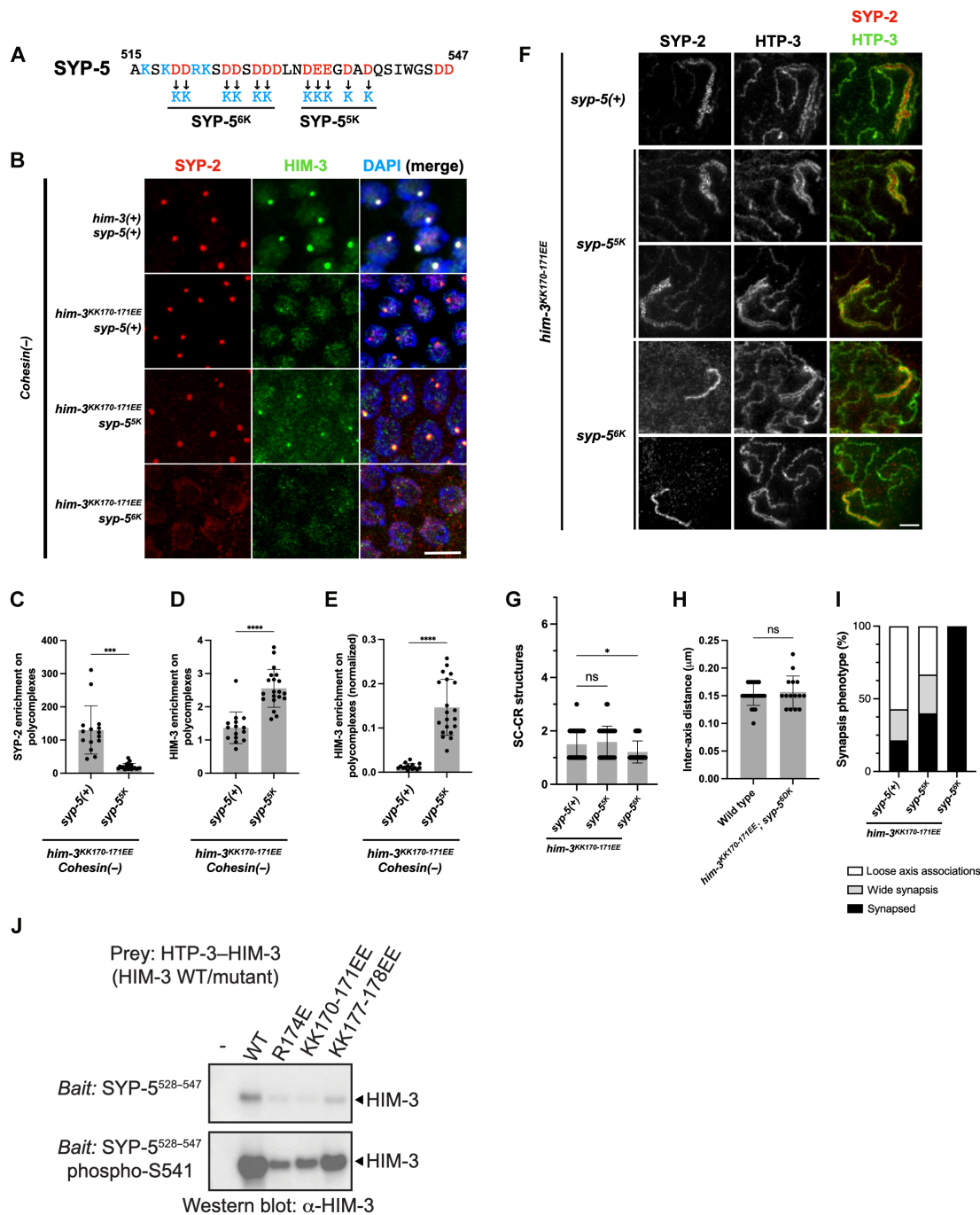


**Fig. 4. The C terminus of SYP-5 contributes to SC-CR interactions with the axis.** (A) The C terminus of SYP-5 (amino acids 515 to 547), with positively and negatively charged residues colored in blue and red, respectively, and charge reversing mutations below. (B) Pachytene nuclei of the indicated genotypes stained for the SC-CR component SYP-2 (red) and the axis component HIM-3 (green). The merged images on the right also show DNA (DAPI, blue). The *syp-5*<sup>56K</sup> mutant fails to form polycomplexes, likely due to perturbed self-interactions of the SC-CR. Scale bar, 2 μm. See fig. S6A for images of the gonads. (C to E) Quantification of the enrichment of SYP-2 and HIM-3 to polycomplexes. While the SC-CR is less enriched at polycomplexes in *syp-5*<sup>56K</sup> animals, these polycomplexes recruit more HIM-3. In (E), HIM-3 enrichment is normalized to SYP-2 enrichment. (F) STED microscopy images of pachytene nuclei stained for SYP-2 (red in the merged image) and the axis component HTP-3 (green). Scale bar, 1 μm. (G) The number of SC-CR structures per pachytene nuclei in the indicated genotypes. (H) Inter-axes distance in the indicated genotypes, measured from nuclei stained as in (F). Distance was measured only for *him-3*<sup>KK170-171EE</sup> *syp-5*<sup>56K</sup> mutants, where the parallel axes exhibited unilamellar SC-CR staining, and is compared to the data from Fig. 3H. (I) Quantification of synapsis phenotypes in STED images, as shown in (F). See Fig. 3G for more details. (J) Anti-HIM-3 Western blot showing the interaction of purified HTP-3-HIM-3 complex containing His<sub>6</sub>-tagged HTP-3 and wild-type (WT) HIM-3, which served as “prey,” with “bait” biotinylated peptides spanning residues 528 to 547 of SYP-5, either unmodified or phosphorylated at S541 (SYP-5 Phos). The interaction was qualitatively weaker with charge reversal mutations in HIM-3. See fig. S8 for complete blots and additional controls. See Materials and Methods for full statistical information.



SC-CR that failed to extend to the entire length of the chromosome (Fig. 3 and fig. S13).

To explore whether thermodynamically driven assembly underlies synapsis, we developed a free energy-based model. Our model incorporates the dimensions of meiotic nuclei and chromosomes in worms (Fig. 5A; see Supplementary Text for a full description of the model). An important quantity in our model is the condensate volume,  $V_c$ . We measured  $V_c$  for polycomplexes ( $\sim 0.05 \mu\text{m}^3$ ; Fig. 5E) and found it to be somewhat smaller than the volume of the assembled SC-CR on chromosomes ( $\sim 0.1 \mu\text{m}^3$ ; Fig. 5A). That is expected given the affinity between the axes and the SC-CR, which would allow recruiting more SC-CR material. Since volume is not easy to measure in fluorescent images, we also used the fraction of SC-CR molecules in condensates, either polycomplexes or assembled synaptonemal complex, as a proxy for  $V_c$  (e.g., in Fig. 5D).

Our model includes energetic terms for two key aspects of synaptonemal complex assembly. The first is the binding of SC-CR molecules to the axis. This depends on the binding energy between SYP-5 (together with other SC-CR components) and HIM-3 (and potentially other axis components), denoted by  $e_{\text{SH}}$ , as well as the number of interacting axis and SC-CR molecules. Each chromosome harbors a limited number of HIM-3 molecules ( $\sim 500$ ), which, in turn, allow for  $\sim 500$  associated SC-CR molecules. The second free energy term incorporates the interfacial energy between the SC-CR and the nucleoplasm, which depends on attractive binding energy among SYP-5 molecules (and other SC-CR components), denoted by  $e_{\text{SS}}$ , and on the minimization of the SC-CR–nucleoplasm interfacial area. The morphology of the SC-CR is therefore defined by the balance between the energetic benefit of surface binding to the axes (adsorption) and the free energy penalty of having a larger surface area for assembled synaptonemal complex threads versus a spherical polycomplex. While we cannot directly measure  $e_{\text{SS}}$  and  $e_{\text{SH}}$ , our modeling reveals that the pertinent effects on synaptonemal complex assembly are captured by the ratio between these two entities, which we denote as  $\alpha = \frac{e_{\text{SH}}}{e_{\text{SS}}}$ .

### Synaptonemal complex assembly model recapitulates empirical observations of physiological and perturbed meiosis

The parameterized model captures multiple aspects of wild-type and mutant synapsis. First, we minimized the total free energy in the system when the condensate volume  $V_c$  is constant. This resulted in a monotonic relationship between  $\alpha$  and the number of synapsed chromosomes (Fig. 6A). Using this graph, the six synapsed chromosomes in wild-type worms yield  $\alpha > 1.2$ . Similarly, the  $\sim 3$  synapsed chromosomes in *him-3<sup>R174E</sup>* worms translate to  $\alpha = 1.0$ . Given that the mutation is in an axes component, this reduction in  $\alpha$  likely reflects weaker  $e_{\text{SH}}$ .

Many of the conditions discussed here affect both  $\alpha$  and  $V_c$ . To capture these complexities, we plotted the result of the model as a contour plot that links  $\alpha$  and  $V_c$  to the number of synapsed chromosomes (Fig. 6B; note that Fig. 6A represents a simplified case, with  $V_c$  held constant at  $V_c = 0.1 \mu\text{m}^3$ ). The black curves denote the minimal values of  $\alpha$  and  $V_c$  that would allow the indicated number of chromosomes to synapse. On the contour plot, the wild-type and *him-3<sup>R174E</sup>* conditions are noted with green and blue asterisks, respectively, and *him-3<sup>KK170-171EE</sup>* worms, with an even lower values of  $\alpha$  and  $V_c$  (Figs. 2 and 5D), is denoted with a red asterisk.

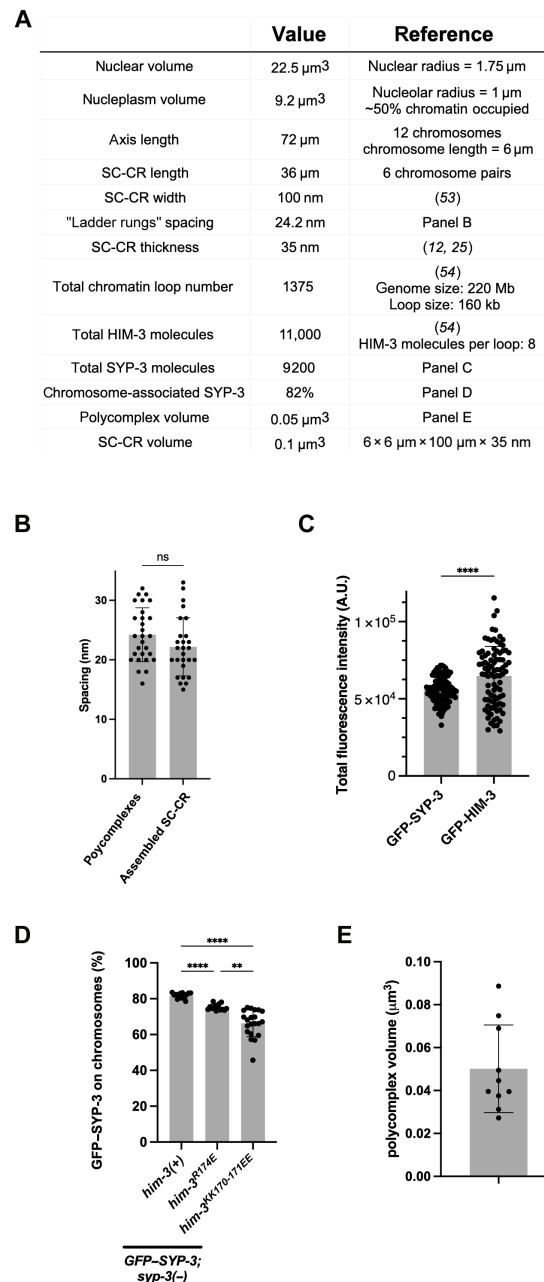


**Fig. 5. Parameters for the thermodynamic model of synaptonemal complex assembly.** (A) Parameters used to model synaptonemal complex assembly. Sources: (12, 25, 52, 53). (B) Distance between the "ladder rungs" in negative stain electron microscopy images from (17). Each point represents an individual measurement between adjacent "rungs."  $N = 28$  and  $27$  for polycomplexes and assembled SC-CR. Welch's  $t$  test  $P = 0.12$ . (C) Total nuclear fluorescence of GFP–HIM-3 and GFP–SYP-3 in pachytene nuclei, yielding a ratio of 1:1.2 GFP–SYP-3 to GFP–HIM-3.  $N = 100$  and  $90$  for GFP–SYP-3 and GFP–HIM-3. Welch's  $t$  test  $P < 0.0001$ . (D) The fraction of GFP–SYP-3 on chromosomes in animals of the indicated genotypes is significantly lower in *him-3<sup>R174E</sup>* and *him-3<sup>KK170-171EE</sup>* mutants.  $N = 15$ ,  $15$ , and  $21$  for *him-3(+)*, *him-3<sup>R174E</sup>*, and *him-3<sup>KK170-171EE</sup>*. Brown-Forsythe and Welch ANOVA  $P[\text{him-3}(+) \text{ versus } \text{him-3<sup>KK107-171EE</sup>}] < 0.0001$ ;  $P[\text{him-3}(+) \text{ versus } \text{him-3<sup>KK107-171EE</sup>}] < 0.0001$ ;  $P[\text{him-3}(+) \text{ versus } \text{him-3<sup>KK107-171EE</sup>}] = 0.0011$ . (E) Polycomplex volume calculated based on the dimensions of polycomplexes in negative stain electron microscopy images from (17). Given the mostly spherical appearance of polycomplexes, the  $z$  dimension is assumed to be the average of the widths and height. Each point indicates a single polycomplex.  $N = 10$ . A.U., arbitrary units.

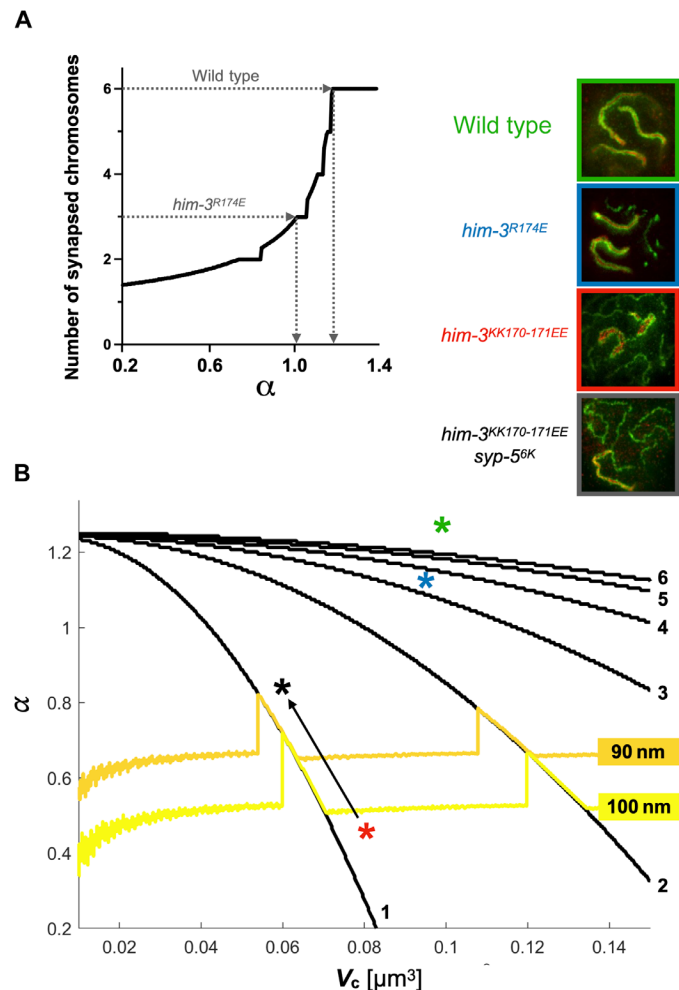


**Fig. 6. Results of the thermodynamic model of synaptonemal complex assembly.** (A) Predicted number of synapsed chromosomes as a function of  $\alpha = \frac{c_{SH}}{c_{SS}}$ . The condensate volume is held constant  $V_c = 0.1 \mu\text{m}^3$ . Dashed arrows indicate how the number of synapsed chromosomes in wild type and  $him-3^{R174E}$  allows to deduce the values of  $\alpha$ . (For simplicity, we ignore here the slight reduction (8%) in  $V_c$  in  $him-3^{R174E}$  worms.) (B) Contour plot of the predicted number of synapsed chromosomes (black lines) as a function of  $V_c$  and  $\alpha$ . The orange and yellow lines indicate threshold SC-CR thickness of 90 and 100 nm, respectively, derived based on the total condensate volume, the dimensions of the SC-CR, and the number of synapsed chromosomes. The green, blue, and red asterisks denote the position of wild-type,  $him-3^{R174E}$ , and  $him-3^{KK170-171EE}$  worms, respectively. The black arrow and asterisk indicate the effect of combining the *syp-5* mutations with  $him-3^{KK170-171EE}$ . Top right: Example images of the mutations shown on the contour plot, with the axis stained in green and the SC-CR in red. See Supplementary Text for more details.

The contour plot also captures information about SC-CR morphology. By dividing the condensate volume by the number of synapsed chromosomes, we deduce the predicted “thickness” of the SC-CR (i.e., the amount of material packed between the two parallel axes). Consistent with the large number of SC-CR molecules per chromosome (fig. S11F), the thickness of the SC-CR in  $him-3^{KK170-171EE}$  worms is predicted to be  $>100$  nm (Fig. 6B; thickness thresholds of 90 and 100 nm are shown as orange and yellow lines, respectively). Notably, the inter-axes distance in  $him-3^{KK170-171EE}$  worms becomes variable, and the SC-CR adopts an ultrastructure resembling polycomplexes [Fig. 3 and fig.

S5; (17, 21)]. This suggests that only a limited amount of SC-CR material could be sandwiched between the axes while maintaining a native synaptonemal complex morphology; beyond this amount, the SC-CR forms a multilamellar structure.

We could similarly overlay on the contour plot the effects of other experimental perturbations. For instance, the charge-swap mutations in *syp-5* that partially suppress the effects of  $him-3^{KK170-171EE}$  represent diagonal upward-left vectors relative to the  $him-3^{KK170-171EE}$  single mutant (lower  $V_c$  and larger  $\alpha$ ; black arrow in Fig. 6B). This vector would bring the thickness of the condensate below the threshold of multilamellar synapsis, consistent with our empirical observations of restored SC-CR morphology in the charge-swap scenario (Fig. 4). Similarly, we model the effects of the temperature-sensitive *syp-1*<sup>K42E</sup> mutation, which destabilizes the SC-CR [fig. S11A; (32)], and the impact of lowering the abundance of SC-CR subunits (fig. S12; see Supplementary Text for full details).

Our ability to recapitulate a variety of experimental data using our free energy-based model indicates that an active mechanism (e.g., polymerization) need not be invoked in the assembly of the synaptonemal complex. Instead, our model indicates that wetting of the axes by the SC-CR can confer selective assembly of the synaptonemal complex between homologs and, by extension, the marked chromosome reorganization necessary to align the homologs.

## DISCUSSION

In this study, we identified a molecular contact between the axis and the SC-CR, which allowed us to explore the mechanism of synaptonemal complex assembly. Molecular genetic analysis combined with in vivo and in vitro experiments revealed an electrostatic interface between a positive patch on the HIM-3 HORMA domain and the negatively charged C terminus of SYP-5. The residual SC-CR-axis association in worms lacking HIM-3 altogether (Fig. 3F) suggests that the HIM-3-SYP-5 interaction acts together with additional contacts to form the axis-SC-CR interface.

The HIM-3 positive patch is conserved in divergent eukaryotic lineages (fig. S2, B and C). Also conserved are the dimensions and ultrastructure of the synaptonemal complex (4, 11) and the SC-CR's dynamic behaviors (17) and its ability to form polycomplexes (21). These observations suggest that the mechanism of synaptonemal complex assembly—wetting of axes by the SC-CR—is likely to be conserved as well. The primary sequence of SC-CR subunits is highly divergent within and between lineages (33), suggesting that sequence alignment by itself might not be sufficient to reveal the SC-CR side of the interface. Nevertheless, our observations suggest that negatively charged regions in SC-CR components could carry an analogous functional role to the C terminus of SYP-5. In some organisms, meiotic HORMA proteins are depleted from the axes following synaptonemal complex assembly (20, 27). However, even in these cases, HORMA proteins are required for synaptonemal complex assembly. An attractive hypothesis is that, following initial assembly, the SC-CR is further stabilized by additional proteins or substructures, rendering it less reliant on stabilization by the axis. Electron micrographs in some species (but not worms) reveal an additional “backbone” in the middle of the SC-CR, called the central element, that was hypothesized to help stabilize the synaptonemal complex (4, 11).

The ability to experimentally modulate the affinity between the SC-CR and the axis allowed us to test mechanisms of synaptonemal complex assembly. The liquid-like properties of the SC-CR, as

demonstrated by the dynamic exchange of subunits and an ability to form droplet-like polycomplexes, led us to hypothesize that it assembles by wetting two HIM-3–coated axes. Wetting, which relies on binding (adsorption) to the axes and self-interactions between SC-CR subunits (condensation), allows the concomitant spread to the entire chromosome and the generation of adhesive forces between the homologous chromosomes. Supporting this idea, a thermodynamic model that assumes only self-interactions between SC-CR subunits and binding interactions between the SC-CR and the axis was able to recapitulate the phenotypes of weakening axis–SC-CR and intra–SC-CR interactions (Figs. 5D and 6 and figs. S10 and S11) and of lowering SC-CR levels (fig. S12).

Our synaptonemal complex assembly model provides an elegant explanation for the association of SC-CR exclusively with paired axes (34). While the SC-CR has an affinity for the axes, binding to unpaired axes provides a small energetic advantage compared with SC-CR condensation. Stable association with axes only occurs in the context of a fully assembled synaptonemal complex, where SC-CR subunits form a condensate that wets the axes. Weakening SC-CR self-association could expose the tendency of SC-CR molecules to bind unpaired axes. Two independent SC-CR mutations that weaken intra–SC-CR associations also lead to SC-CR association with unpaired axes [the aforementioned *syp-1*<sup>K42E</sup> and *syp-3(me42)*; fig. S11A; (17, 32, 35)].

Severe perturbations of axis–SC-CR interactions [*him-3*<sup>KK170-171EE</sup> or *him-3(-)*] led to the formation of large SC-CR aggregates that are associated with axes. These aggregates place the axes >400 nm apart—too far to be spanned by a single SC-CR lamella (~150 nm; Fig. 3F). The potential to form such a structure suggests that the wild-type scenario—where unilamellar SC-CR coats the axes from end to end—reflects a tightly regulated balance between axis–SC-CR binding and the interfacial tension of SC-CR condensates. In addition to enabling end-to-end synapsis of parental chromosomes, such a balance could also counter the thermodynamic drive of liquids to minimize surface tension [e.g., through the process of Ostwald ripening; (2)]. Axis wetting therefore underlies persistent and complete synapsis—the maintenance of independent SC-CR compartments, one on each chromosome—during the many hours in which the synaptonemal complex remains assembled.

A unilamellar SC-CR has crucial functional implications. Complete synapsis ensures two fundamental characteristics of meiotic crossovers: (i) All chromosomes undergo at least one crossover, and (ii) crossovers only occur between homologous chromosomes. The specter of multiple axes interacting with large SC-CR aggregates (Fig. 3F) is likely to prevent synapsis of all chromosomes by sequestering SC-CR material. It could also allow ectopic exchanges between nonhomologous chromosomes and, consequently, karyotype aberrations and aneuploidy. The limited surface area of a unilamellar SC-CR, together with repulsive forces between chromatin masses (36), could limit the number of interacting axes to no more than two. Such a mechanism to prevent multichromosome associations can help explain the evolutionary conservation of the synaptonemal complex, which exhibits only minor ultrastructural variations between species with order-of-magnitude differences in genome size and chromosome number (4, 11).

Our thermodynamic model groups together the distinctive affinities that drive SC-CR self-interactions: stacking of SC-CR subunits and the lateral attachments between SC-CR lamellae. The spherical morphology of stacked ladder-like lamellae in polycomplexes suggests a balance with the anisotropic elements (ladder-like assembly) and

the potentially isotropic attractive interactions among SC-CR proteins. This spherical morphology is distinct from mitotic spindles (37) but more akin to drops of fragmented amyloid fibrils in yeast (38). The nonspherical polycomplexes that form in some organisms (21) and in certain mutant backgrounds [e.g., (32)] provide an opportunity for future studies of the balance between stacking and lateral interactions. It is also worth noting that while our thermodynamic modeling focuses on the near-equilibrium state eventually reached by the SC-CR, the kinetics of synapsis are likely to be affected by numerous active processes. These include motor-driven chromosome motions that occur in meiotic prophase in many organisms (4). Dynein-driven chromosome motions in worms affect the rate of synapsis (in addition to other aspects of homolog pairing), but they are not required for SC-CR assembly per se (15, 39), consistent with the assumptions of our model.

Cell biologists have identified numerous supramolecular assemblies in the nucleus (40). Many of these structures have been suggested to exert force and movement on the genome to organize it and thus tightly regulate biological processes ranging from transcription to genome maintenance. The in vitro and in vivo material properties of many such structures have been a focus of recent probing. However, only rarely has it been shown that a specific material state of a supramolecular assembly (e.g., a liquid) underlies the nuclear-scale maneuvering of chromosomes in the nucleus (2, 41). Synaptonemal complex assembly through wetting demonstrates that the liquid properties of the SC-CR underlie a core component of meiosis—the large-scale chromosome reorganization that brings homologous chromosomes together.

## MATERIALS AND METHODS

### Worm strains and CRISPR

Worms were grown under standard conditions (42). Unless otherwise noted, all worms were grown at 20°C. All strains used in this study are listed in table S1. CRISPR was performed as previously described (32), with guide RNA and repair templates listed in table S2. All new alleles were confirmed by Sanger sequencing.

### Structural models of HORMA domain-containing proteins

Protein Data Bank (PDB) files for HTP-1, HIM-3 (26), and *Homo sapiens* HORMAD1 (43) were downloaded from the RCSB PDB (<https://www.rcsb.org/>) and uploaded into ChimeraX (44). Electrostatic models of surface charge were created with the Surfaces tab on ChimeraX. Models of *him-3* charge reversal mutants were created using the Rotamers tab and changing the specified amino acids to aspartic acid residues with the “best predicted” position. A predicted structure of the HORMA domain of HTP-3 was generated in AlphaFold (45) without the C-terminal tail. The best-predicted structure was used. A predicted structure of *S. cerevisiae* Hop1 (UniProt ID P20050) was downloaded from the AlphaFold Protein Structure Database (<https://alphafold.ebi.ac.uk/>) (46).

### Immunofluorescence and fluorescence measurements on polycomplexes

Immunofluorescence was performed as described in (32). Images were acquired with a Zeiss LSM880 microscope equipped with an AiryScan and a 63× 1.4 numerical aperture oil objective. The laser powers were kept the same at 1.5% 633 nm, 0.3% 561 nm, 2.2% 488 nm, and 4.5% 405 nm. The antibodies used were guinea pig anti-HTP-3 (34), rabbit



anti-SYP-5 (29), chicken anti-HIM-3 (29), and rabbit anti-SYP-2 (47), with appropriate secondary antibodies (Jackson ImmunoResearch). Line scans were analyzed in ZEN Blue 3.0 (Zeiss) on a single z-slice where the polycomplex has the highest fluorescence. The average fluorescence inside the polycomplex and in the nucleoplasm (outside the polycomplex) were used to determine enrichment on polycomplexes. To normalize, the enrichment of the axis component was divided by the enrichment of the SC-CR component.

### Meiotic phenotypes

Progeny and male counts were performed as in (32). Synapsed chromosomes were counted in maximum-intensity projection images of gonads stained for an SC-CR component (SYP-2 or SYP-5). Chiasmata were counted as in (32). Synapsis phenotypes were determined on STED images and were confirmed with line scans to determine that the inter-axis distance was greater than 150 nm.

### STED imaging

Immunofluorescence slides were made as above, with the following modifications. We used rabbit anti-SYP-5 (29), rabbit anti-SYP-2 (29), and guinea pig anti-HTP-3 primary antibodies and STAR RED anti-rabbit (Abberior; 1:200) and Alexa Fluor 594 anti-guinea pig (Jackson ImmunoResearch; 1:200) as secondary antibodies. We used liquid mount (Abberior) as a mounting media. Imaging on STEDYCON was done as in (48). Line scans were used to determine the distance between axes, as described in (48).

### Live gonad imaging

Live imaging of gonads was performed essentially as described in (49). Briefly, 2% agarose pads soaked with embryonic culture medium (ECM; 84% Leibowitz L-15 without phenol red, 9.3% fetal bovine serum, 0.01% levamisole, and 2 mM EGTA) for ~20 min. Worms were dissected in 20  $\mu$ l of ECM supplemented with Hoechst 33342 (1:200). The slides were sealed with VALAP (1:1:1 mix of Vaseline, lanolin and paraffin) and imaged using 4% 488 laser power and 4.5% 405 laser power. Images were processed using Imaris 10.0 (Bitplane). Five nuclei from each gonad were cropped, and a mask for the 488 channel was made. The mask was applied using the default setting but was manually adjusted as appropriate, particularly in some genotypes [*sy-3* RNA interference (RNAi) and *htp-3(-)*].

### RNA interference

RNAi was performed as described in (5). Briefly, *sy-3* (F39H2.4) and RNAi control (pL4440) plasmids from the Ahringer laboratory RNAi library (50) were grown overnight in LB + carbenicillin at 37°C, spread on RNAi plates [nematode growth media (NGM) + carbenicillin + isopropyl- $\beta$ -D-thiogalactopyranoside (IPTG)], and incubated overnight at 37°C. L4 worms were placed on RNAi plates and grown for 24 hours at 20°C. Live gonads were imaged as described above.

### CRISPR

CRISPR-Cas9 injections were performed essentially as described in (32), with the templates and guides listed in table S1. Correct repair was confirmed by Sanger sequencing.

### Protein purification

Codon-optimized genes encoding His<sub>6</sub>-HTP-3 residues 2 to 739 and HIM-3 residues 1 to 291 were cloned as a polycistronic cassette

into a single vector (UCB Macrolab 2B-T; Addgene #29666), resulting in an N-terminal His<sub>6</sub>-tag fused to HTP-3 (26). For expression of HTP-3 or HIM-3 alone, single genes were cloned into the same vector. Expression vectors were transformed into *Escherichia coli* Rosetta pLysS (EMD Millipore) and grown at 37°C to an optical density at 600 nm of 0.5, then expression was induced with addition of 0.2 mM IPTG, growth temperature was adjusted to 20°C, and growth continued for 16 hours. Cells were harvested by centrifugation, resuspended in lysis buffer [20 mM Hepes (pH 7), 300 mM NaCl, 10% glycerol, 5 mM MgCl<sub>2</sub>, 5 mM imidazole, and 5 mM  $\beta$ -ME ( $\beta$ -mercaptoethanol)], and lysed in a sonicator (Branson Sonifier), and then the lysate was clarified by centrifugation. Expressed proteins were purified from clarified lysates via affinity chromatography (Ni-NTA Superflow resin; QIAGEN) in lysis buffer. Lysate was incubated with nickel resin for 30 min and then washed with lysis buffer with 20 mM imidazole. Protein was eluted in lysis buffer with 500 mM imidazole. Protein fractions were then pooled and diluted to 100 mM NaCl in 20 mM Hepes (pH 7), 10% glycerol, and 5 mM  $\beta$ -ME and loaded onto an anion exchange column (HiTrap Q HP; Cytiva). Protein was eluted with a gradient from 100 mM NaCl to 1 M NaCl, and fractions containing the desired proteins were pooled, concentrated in a centrifugal concentrator (Amicon Ultra; EMD Millipore), and loaded onto a size exclusion column (Superdex 200 Increase 10/300 GL; Cytiva) in buffer containing 20 mM Hepes (pH 7), 300 mM NaCl, 10% glycerol, and 1 mM dithiothreitol. Fractions containing the desired proteins were pooled, concentrated, and stored at -80°C until needed.

### Pulldowns of HIM-3 and SYP-5

SYP-5 peptides spanning residues 528 to 547 (sequence: DDD-LNDEEGDADQSIWGSDD) with S541 phosphorylated and unphosphorylated were purchased from Biomatik with an N-terminal biotin label. Purified HTP-3-HIM-3 was incubated with SYP-5 phosphorylated and unphosphorylated peptides (10  $\mu$ g each, 25  $\mu$ l each) in pulldown buffer 20 mM Tris-HCl (pH 8), 150 mM NaCl, 5% glycerol, 0.01% NP-40, and 0.5 mM  $\beta$ -ME for 30 min at room temperature with rotation. Magnetic streptavidin resin (streptavidin beads; Vazyme) was added to protein mixture and incubated at room temperature for an additional 15 min with rotation. After incubation, beads were washed with 1 ml of pulldown buffer and incubated at room temperature with rotation for 5 min. Reaction mixture was then incubated on a magnetic strip, and the supernatant was removed. Pulldown buffer was added, and cycles of incubating beads on a magnetic strip and the removing supernatant were followed until three washes were completed. Streptavidin beads were resuspended in 20  $\mu$ l of 2 $\times$  SDS loading buffer with 25 mM biotin and boiled. Samples were loaded onto SDS-polyacrylamide gel electrophoresis gel for protein identification followed by Western blotting. For Western blot, proteins were transferred to polyvinylidene difluoride membrane (Bio-Rad Trans-Blot Turbo) and then blocked with 3% nonfat dry milk and blotted. Blots were imaged with the Bio-Rad ChemiDoc system using filters to image horseradish peroxidase (HRP) activity. Antibodies used were chicken anti-HIM-3 primary antibody (gift from Y. Kim) at 1:5000 dilution and donkey anti-chicken HRP-conjugated secondary antibody (Jackson ImmunoResearch Laboratories Inc. #703-035-155) at 1:30,000 dilution.

### Statistical analysis

All statistical analysis was done in Prism 10.0 (GraphPad). In all figures, significant *P* values are indicated as follows: (\*) for  $0.05 \geq P > 0.01$ ,

(\*\*) for  $0.01 \geq P > 0.001$ , (\*\*\*) for  $0.001 \geq P > 0.0001$ , and \*\*\*\* $P \leq 0.0001$ .

### Statistical information for figures

Figure 3A:  $N = 10, 7$ , and  $10$  broods from wild type,  $him-3^{R174E}$ , and  $him-3^{KK170-171EE}$ . Brown-Forsythe and Welch analysis of variance (ANOVA)  $P(\text{wild type versus } him-3^{R174E}) < 0.0001$ ;  $P(\text{wild type versus } him-3^{KK170-171EE}) < 0.0001$ ;  $P(him-3^{R174E} \text{ versus } him-3^{KK170-171EE}) = 0.058$ .

Figure 3B:  $N = 10, 7$ , and  $10$  broods from wild type,  $him-3^{R174E}$ , and  $him-3^{KK170-171EE}$ . Brown-Forsythe and Welch ANOVA  $P(\text{wild type versus } him-3^{R174E}) < 0.0001$ ;  $P(\text{wild type versus } him-3^{KK170-171EE}) < 0.0001$ ;  $P(him-3^{R174E} \text{ versus } him-3^{KK170-171EE}) = 0.058$ .

Figure 3D:  $N = 56, 58$ , and  $58$  nuclei from wild type,  $him-3^{R174E}$ , and  $him-3^{KK170-171EE}$ . Brown-Forsythe and Welch ANOVA  $P(\text{wild type versus } him-3^{R174E}) < 0.0001$ ;  $P(\text{wild type versus } him-3^{KK170-171EE}) < 0.0001$ .

Figure 3E:  $N = 15, 53$ , and  $34$  diakinesis nuclei from wild type,  $him-3^{R174E}$ , and  $him-3^{KK170-171EE}$ . Brown-Forsythe and Welch ANOVA  $P(\text{wild type versus } him-3^{R174E}) < 0.0001$ ;  $P(\text{wild type versus } him-3^{KK170-171EE}) < 0.0001$ .

Figure 3H:  $N = 24$  and  $21$  chromosomes from wild type and  $him-3^{R174E}$ . Brown-Forsythe and Welch ANOVA  $P(\text{wild type versus } him-3^{R174E}) = 0.99$ .

Figure 4 (C to E):  $N = 15$  and  $20$  nuclei for  $syp-5(+)$  and  $syp-5^{5K}$ . (C) Brown-Forsythe and Welch ANOVA  $P = 0.0006$ . (D) Brown-Forsythe and Welch ANOVA  $P < 0.0001$ . (E) Brown-Forsythe and Welch ANOVA  $P < 0.0001$ .

Figure 4G:  $N = 58, 41$ , and  $52$  nuclei for  $syp-5(+)$ ,  $syp-5^{5K}$ , and  $syp-5^{6K}$ . Brown-Forsythe and Welch ANOVA  $P[syp-5(+)$  versus  $syp-5^{5K}] = 0.99$ ;  $P[syp-5(+)$  versus  $syp-5^{6K}] = 0.029$ .

Figure 4H:  $N = 24$  and  $15$  for wild type and  $him-3^{KK170-171EE}$   $syp-5^{6K}$ . Brown-Forsythe and Welch ANOVA  $P = 0.99$ .

### Supplementary Materials

#### The PDF file includes:

Supplementary Text  
Figs. S1 to S17  
Tables S1 and S2  
Legends for data S1 to S3  
References

#### Other Supplementary Material for this manuscript includes the following:

Data S1 to S3

### REFERENCES AND NOTES

- C. P. Brangwynne, C. R. Eckmann, D. S. Courson, A. Rybarska, C. Hoege, J. Gharakhani, F. Jülicher, A. A. Hyman, Germline P granules are liquid droplets that localize by controlled dissolution/condensation. *Science* **324**, 1729–1732 (2009).
- B. Gouveia, Y. Kim, J. W. Shaevitz, S. Petry, H. A. Stone, C. P. Brangwynne, Capillary forces generated by biomolecular condensates. *Nature* **609**, 255–264 (2022).
- A. R. Strom, Y. Kim, H. Zhao, Y.-C. Chang, N. D. Orlovsky, A. Košmrlj, C. Storm, C. P. Brangwynne, Condensate interfacial forces reposition DNA loci and probe chromatin viscoelasticity. *Cell* **187**, 5282–5297.e20 (2024).
- D. Zickler, N. Kleckner, Meiosis: Dances between homologs. *Annu. Rev. Genet.* **57**, 1–63 (2023).
- D. E. Libuda, S. Uzawa, B. J. Meyer, A. M. Villeneuve, Meiotic chromosome structures constrain and respond to designation of crossover sites. *Nature* **502**, 703–706 (2013).
- S. Durand, Q. Lian, J. Jing, M. Ernst, M. Grelon, D. Zwicker, R. Mercier, Joint control of meiotic crossover patterning by the synaptonemal complex and HEI10 dosage. *Nat. Commun.* **13**, 5999 (2022).
- L. Zhang, W. Stauffer, D. Zwicker, A. F. Dernburg, Crossover patterning through kinase-regulated condensation and coarsening of recombination nodules. *bioRxiv* 457865 [Preprint] (2021). <https://doi.org/10.1101/2021.08.26.457865>.
- J. A. Fozard, C. Morgan, M. Howard, Coarsening dynamics can explain meiotic crossover patterning in both the presence and absence of the synaptonemal complex. *eLife* **12**, e79408 (2023).
- C. Morgan, J. A. Fozard, M. Hartley, I. R. Henderson, K. Bomblies, M. Howard, Diffusion-mediated HEI10 coarsening can explain meiotic crossover positioning in Arabidopsis. *Nat. Commun.* **12**, 4674 (2021).
- L. von Diezmann, C. Bristow, O. Rog, Diffusion within the synaptonemal complex can account for signal transduction along meiotic chromosomes. *Mol. Biol. Cell* **35**, ar148 (2024).
- S. L. Page, R. S. Hawley, The genetics and molecular biology of the synaptonemal complex. *Annu. Rev. Cell Dev. Biol.* **20**, 525–558 (2004).
- S. Köhler, M. Wojcik, K. Xu, A. F. Dernburg, The interaction of crossover formation and the dynamic architecture of the synaptonemal complex during meiosis. *bioRxiv* 947804 [Preprint] (2020). <https://doi.org/10.1101/2020.02.16.947804>.
- K. Schild-Prüfert, T. T. Saito, S. Smolnikov, Y. Gu, M. Hincapie, D. E. Hill, M. Vidal, K. McDonald, M. P. Colaiácovo, Organization of the synaptonemal complex during meiosis in *Caenorhabditis elegans*. *Genetics* **189**, 411–421 (2011).
- K. Schücker, T. Holm, C. Franke, M. Sauer, R. Benavente, Elucidation of synaptonemal complex organization by super-resolution imaging with isotropic resolution. *Proc. Natl. Acad. Sci. U.S.A.* **112**, 2029–2033 (2015).
- O. Rog, A. F. Dernburg, Direct visualization reveals kinetics of meiotic chromosome synapsis. *Cell Rep.* **10**, 1639–1645 (2015).
- M. G. Pollard, B. Rockmill, A. Oke, C. M. Anderson, J. C. Fung, Kinetic analysis of synaptonemal complex dynamics during meiosis of yeast *Saccharomyces cerevisiae* reveals biphasic growth and abortive disassembly. *Front. Cell. Dev. Biol.* **11**, 1098468 (2023).
- O. Rog, S. Köhler, A. F. Dernburg, The synaptonemal complex has liquid crystalline properties and spatially regulates meiotic recombination factors. *eLife* **6**, e21455 (2017).
- S. Nadarajan, T. J. Lambert, E. Altendorfer, J. Gao, M. D. Blower, J. C. Waters, M. P. Colaiácovo, Polo-like kinase-dependent phosphorylation of the synaptonemal complex protein SYP-4 regulates double-strand break formation through a negative feedback loop. *eLife* **6**, e23437 (2017).
- D. Pattabiraman, B. Roelens, A. Woglar, A. M. Villeneuve, Meiotic recombination modulates the structure and dynamics of the synaptonemal complex during *C. elegans* meiosis. *PLOS Genet.* **13**, e1006670 (2017).
- S. G. Gordon, O. Rog, Building the synaptonemal complex: Molecular interactions between the axis and the central region. *PLOS Genet.* **19**, e1010822 (2023).
- S. E. Hughes, R. S. Hawley, Alternative synaptonemal complex structures: Too much of a good thing? *Trends Genet.* **36**, 833–844 (2020).
- M. Sym, G. S. Roeder, Zip1-induced changes in synaptonemal complex structure and polycomplex assembly. *J. Cell Biol.* **128**, 455–466 (1995).
- A. F. Severson, B. J. Meyer, Divergent kleisin subunits of cohesin specify mechanisms to tether and release meiotic chromosomes. *eLife* **3**, e03467 (2014).
- Y. Kim, N. Kostow, A. F. Dernburg, The chromosome axis mediates feedback control of CHK-2 to ensure crossover formation in *C. elegans*. *Dev. Cell* **35**, 247–261 (2015).
- S. Köhler, M. Wojcik, K. Xu, A. F. Dernburg, Superresolution microscopy reveals the three-dimensional organization of meiotic chromosome axes in intact *Caenorhabditis elegans* tissue. *Proc. Natl. Acad. Sci. U.S.A.* **114**, E4734–E4743 (2017).
- Y. Kim, S. C. Rosenberg, C. L. Kugel, N. Kostow, O. Rog, V. Davydov, T. Y. Su, A. F. Dernburg, K. D. Corbett, The chromosome axis controls meiotic events through a hierarchical assembly of HORMA domain proteins. *Dev. Cell* **31**, 487–502 (2014).
- S. N. Ur, K. D. Corbett, Architecture and dynamics of meiotic chromosomes. *Annu. Rev. Genet.* **55**, 497–526 (2021).
- F. Couteau, K. Nabeshima, A. Villeneuve, M. Zetka, A component of *C. elegans* meiotic chromosome axes at the interface of homolog alignment, synapsis, nuclear reorganization, and recombination. *Curr. Biol.* **14**, 585–592 (2004).
- M. E. Hurllock, I. Čavka, L. E. Kursel, J. Haversat, M. Wooten, Z. Nizami, R. Turniansky, P. Hoess, J. Ries, J. G. Gall, O. Rog, S. Köhler, Y. Kim, Identification of novel synaptonemal complex components in *C. elegans*. *J. Cell Biol.* **219**, e201910043 (2020).
- Z. Zhang, S. Xie, R. Wang, S. Guo, Q. Zhao, H. Nie, Y. Liu, F. Zhang, M. Chen, L. Liu, X. Meng, M. Liu, L. Zhao, M. P. Colaiácovo, J. Zhou, J. Gao, Multivalent weak interactions between assembly units drive synaptonemal complex formation. *J. Cell Biol.* **219**, e201910086 (2020).
- A. L. Gold, M. E. Hurllock, A. M. Guevara, L. Y. Z. Isenberg, Y. Kim, Identification of the Polo-like kinase substrate required for homologous synapsis. *J. Cell Biol.* **224**, e202408092 (2025).
- S. G. Gordon, L. E. Kursel, K. Xu, O. Rog, Synaptonemal complex dimerization regulates chromosome alignment and crossover patterning in meiosis. *PLOS Genet.* **17**, e1009205 (2021).
- L. E. Kursel, H. D. Cope, O. Rog, Unconventional conservation reveals structure-function relationships in the synaptonemal complex. *eLife* **10**, e72061 (2021).

34. A. J. MacQueen, C. M. Phillips, N. Bhalla, P. Weiser, A. M. Villeneuve, A. F. Dernburg, Chromosome sites play dual roles to establish homologous synapsis during meiosis in *C. elegans*. *Cell* **123**, 1037–1050 (2005).
35. S. Smolnikov, A. Eizinger, K. Schild-Prufert, A. Hurlburt, K. McDonald, J. Engebrecht, A. M. Villeneuve, M. P. Colaiácovo, SYP-3 restricts synaptonemal complex assembly to bridge paired chromosome axes during meiosis in *Caenorhabditis elegans*. *Genetics* **176**, 2015–2025 (2007).
36. J. F. Marko, E. D. Siggia, Polymer models of meiotic and mitotic chromosomes. *Mol. Biol. Cell* **8**, 2217–2231 (1997).
37. D. Oriola, F. Jülicher, J. Brugués, Active forces shape the metaphase spindle through a mechanical instability. *Proc. Natl. Acad. Sci. U.S.A.* **117**, 16154–16159 (2020).
38. J. Tyedmers, S. Treusch, J. Dong, J. M. McCaffery, B. Bevis, S. Lindquist, Prion induction involves an ancient system for the sequestration of aggregated proteins and heritable changes in prion fragmentation. *Proc. Natl. Acad. Sci. U.S.A.* **107**, 8633–8638 (2010).
39. A. Sato, B. Isaac, C. M. Phillips, R. Rillo, P. M. Carlton, D. J. Wynne, R. A. Kasad, A. F. Dernburg, Cytoskeletal forces span the nuclear envelope to coordinate meiotic chromosome pairing and synapsis. *Cell* **139**, 907–919 (2009).
40. B. R. Sabari, A. Dall'Agnese, R. A. Young, Biomolecular condensates in the nucleus. *Trends Biochem. Sci.* **45**, 961–977 (2020).
41. Y.-C. Chung, L.-C. Tu, Interplay of dynamic genome organization and biomolecular condensates. *Curr. Opin. Cell Biol.* **85**, 102252 (2023).
42. S. Brenner, The genetics of *Caenorhabditis elegans*. *Genetics* **77**, 71–94 (1974).
43. H. Wang, R. Xie, F. Niu, Q. Yang, L. An, C. Wu, X. Liu, X. Yang, Structural and biochemical insights into the interaction mechanism underlying HORMAD1 and its partner proteins. *Structure* **31**, 1578–1588.e3 (2023).
44. E. C. Meng, T. D. Goddard, E. F. Pettersen, G. S. Couch, Z. J. Pearson, J. H. Morris, T. E. Ferrin, UCSF ChimeraX: Tools for structure building and analysis. *Protein Sci.* **32**, e4792 (2023).
45. A. W. Senior, R. Evans, J. Jumper, J. Kirkpatrick, L. Sifre, T. Green, C. Qin, A. Židek, A. W. R. Nelson, A. Bridgland, H. Penadones, S. Petersen, K. Simonyan, S. Crossan, P. Kohli, D. T. Jones, D. Silver, K. Kavukcuoglu, D. Hassabis, Improved protein structure prediction using potentials from deep learning. *Nature* **577**, 706–710 (2020).
46. M. Varadi, D. Bertoni, P. Magana, U. Paramval, I. Pidruchna, M. Radhakrishnan, M. Tsenkov, S. Nair, M. Mirdita, J. Yeo, O. Kovalevskiy, K. Tunyasuvunakool, A. Laydon, A. Židek, H. Tomlinson, D. Hariharan, J. Abrahamson, T. Green, J. Jumper, E. Birney, M. Steinegger, D. Hassabis, S. Velankar, AlphaFold protein structure database in 2024: Providing structure coverage for over 214 million protein sequences. *Nucleic Acids Res.* **52**, D368–D375 (2024).
47. M. P. Colaiácovo, A. J. MacQueen, E. Martinez-Perez, K. McDonald, A. Adamo, A. La Volpe, A. M. Villeneuve, Synaptonemal complex assembly in *C. elegans* is dispensable for loading strand-exchange proteins but critical for proper completion of recombination. *Dev. Cell* **5**, 463–474 (2003).
48. D. E. Almanzar, S. G. Gordon, C. Bristow, A. Hamrick, L. von Diezmann, H. Liu, O. Rog, Meiotic DNA exchanges in *C. elegans* are promoted by proximity to the synaptonemal complex. *Life Sci. Alliance* **6**, e202301906 (2023).
49. L. von Diezmann, O. Rog, Single-molecule tracking of chromatin-associated proteins in the *C. elegans* gonad. *J. Phys. Chem. B* **125**, 6162–6170 (2021).
50. R. S. Kamath, A. G. Fraser, Y. Dong, G. Poulin, R. Durbin, M. Gotta, A. Kanapin, N. Le Bot, S. Moreno, M. Sohrmann, D. P. Welchman, P. Zipperlen, J. Ahringer, Systematic functional analysis of the *Caenorhabditis elegans* genome using RNAi. *Nature* **421**, 231–237 (2003).
51. J. M. Blundon, B. I. Cesar, J. W. Bae, I. Čavka, J. Haversat, J. Ries, S. Köhler, Y. Kim, Skp1 proteins are structural components of the synaptonemal complex in *C. elegans*. *Sci. Adv.* **10**, ead14876 (2024).
52. P. Goldstein, D. E. Slaton, The synaptonemal complexes of *Caenorhabditis elegans*: Comparison of wild-type and mutant strains and pachytene karyotype analysis of wild-type. *Chromosoma* **84**, 585–597 (1982).
53. A. Woglar, K. Yamaya, B. Roelens, A. Boettiger, S. Köhler, A. M. Villeneuve, Quantitative cytogenetics reveals molecular stoichiometry and longitudinal organization of meiotic chromosome axes and loops. *PLOS Biol.* **18**, e3000817 (2020).
54. A. J. MacQueen, M. P. Colaiácovo, K. McDonald, A. M. Villeneuve, Synapsis-dependent and -independent mechanisms stabilize homolog pairing during meiotic prophase in *C. elegans*. *Genes Dev.* **16**, 2428–2442 (2002).
55. S. Smolnikov, K. Schild-Prüfert, M. P. Colaiácovo, A yeast two-hybrid screen for SYP-3 interactors identifies SYP-4, a component required for synaptonemal complex assembly and chiasma formation in *Caenorhabditis elegans* meiosis. *PLOS Genet.* **5**, e1000669 (2009).
56. S. Smolnikov, A. Eizinger, A. Hurlburt, E. Rogers, A. M. Villeneuve, M. P. Colaiácovo, Synapsis-defective mutants reveal a correlation between chromosome conformation and the mode of double-strand break repair during *Caenorhabditis elegans* meiosis. *Genetics* **176**, 2027–2033 (2007).
57. A. W. Fritsch, A. F. Diaz-Delgadillo, O. Adame-Arana, C. Hoege, M. Mittasch, M. Kreising, M. Leaver, A. A. Hyman, F. Jülicher, C. A. Weber, Local thermodynamics govern formation and dissolution of *Caenorhabditis elegans* P granule condensates. *Proc. Natl. Acad. Sci. U.S.A.* **118**, e2102772118 (2021).
58. J. B. Woodruff, B. Ferreira Gomes, P. O. Widlund, J. Mahamid, A. Honigsmann, A. A. Hyman, The centrosome is a selective condensate that nucleates microtubules by concentrating tubulin. *Cell* **169**, 1066–1077.e10 (2017).
59. C. M. Phillips, C. Wong, N. Bhalla, P. M. Carlton, P. Weiser, P. M. Meneely, A. F. Dernburg, HIM-8 binds to the X chromosome pairing center and mediates chromosome-specific meiotic synapsis. *Cell* **123**, 1051–1063 (2005).
60. C. M. Phillips, A. F. Dernburg, A family of zinc-finger proteins is required for chromosome-specific pairing and synapsis during meiosis in *C. elegans*. *Dev. Cell* **11**, 817–829 (2006).
61. F. Baudat, K. Manova, J. P. Yuen, M. Jasin, S. Keeney, Chromosome synapsis defects and sexually dimorphic meiotic progression in mice lacking Spo11. *Mol. Cell* **6**, 989–998 (2000).
62. F.-M. Lin, Y.-J. Lai, H.-J. Shen, Y.-H. Cheng, T.-F. Wang, Yeast axial-element protein, Red1, binds SUMO chains to promote meiotic interhomologue recombination and chromosome synapsis. *EMBO J.* **29**, 586–596 (2010).
63. K. Voelkel-Meiman, S. S. Moustafa, P. Lefrançois, A. M. Villeneuve, A. J. MacQueen, Full-length synaptonemal complex grows continuously during meiotic prophase in budding yeast. *PLOS Genet.* **8**, e1002993 (2012).
64. M. Hayashi, S. Mlynarczyk-Evans, A. M. Villeneuve, The synaptonemal complex shapes the crossover landscape through cooperative assembly, crossover promotion and crossover inhibition during *Caenorhabditis elegans* meiosis. *Genetics* **186**, 45–58 (2010).
65. J.-L. Barrat, J.-P. Hansen, *Basic Concepts for Simple and Complex Liquids* (Cambridge Univ. Press, 2011).
66. W. T. Stauffer, L. Zhang, A. Dernburg, “Diffusion through a liquid crystalline compartment regulates meiotic recombination” in *Biophysics, Biology, and Biophotonics IV: The Crossroads* (SPIE, 2019), vol. 10888, pp. 8–15.

**Acknowledgments:** We would like to thank all members of the Rog lab and M. Horvath for discussions and advice; Y. Kim for discussing data before publication and for antibodies; A. MacQueen for discussion and advice; A. Strom and E. Jorgensen for critical reading of this manuscript; S. Nakiely for editorial work; M. Diaz de la Loza for scientific illustrations; and A. Dernburg for antibodies. Some worm strains were provided by the *Caenorhabditis* Genetics Center, which is funded by NIH Office of Research Infrastructure Programs (P40 OD010440). We acknowledge the HSC Imaging Core for the use of the STED microscope. **Funding:** This work was supported by NIGMS grant R35GM144121 to K.D.C. and NIGMS grant R35GM128804 to O.R. **Author contributions:** S.G.G.: Writing (original draft), conceptualization, investigation, writing (review and editing), methodology, resources, data curation, validation, supervision, formal analysis, project administration, and visualization. A.A.R.: Writing (original draft), conceptualization, investigation, writing (review and editing), methodology, resources, validation, and visualization. Y.G.: Investigation, writing (review and editing), formal analysis, and visualization. O.R.: Writing (original draft), conceptualization, writing (review and editing), methodology, resources, funding acquisition, validation, supervision, formal analysis, project administration, and visualization. C.F.L.: Writing (original draft), conceptualization, writing (review and editing), methodology, formal analysis, project administration, and visualization. K.D.C.: Writing (original draft), conceptualization, writing (review and editing), methodology, funding acquisition, supervision, formal analysis, project administration, and visualization. **Competing interests:** The authors declare that they have no competing interests. **Data and materials availability:** All data needed to evaluate the conclusions in the paper are present in the paper and/or the Supplementary Materials. The following structures were used in this study: *C. elegans* HIM-3 (PDB: 4TRK); *C. elegans* HTP-1 (PDB: 4TZO); *H. sapiens* HORMAD1 (PDB: 8J69).

Submitted 1 October 2024

Accepted 23 January 2025

Published 26 February 2025

10.1126/sciadv.adt5675